Scripta Materialia 271 (2026) 117026

Contents lists available at ScienceDirect

Scripta Materialia

journal homepage: www.journals.elsevier.com/scripta-materialia

Ultra-slow coarsening in precipitation-strengthened refractory high-entropy alloys

R.J. Vikram [a,*], Sandipan Sen [a,*], Liu Yang [a], Michael K. Eusterholz [a,b], Amin Radi [a], Daniel Schliephake [a,b], Jean-Philippe Couzinié [c], Alexander Kauffmann [d,*], Martin Heilmaier [a,*]

[a] Institute for Applied Materials (IAM-WK), Karlsruhe Institute of Technology (KIT), Engelbert-Arnold-Str. 4 76131 Karlsruhe, Germany
[b] Karlsruhe Nano Micro Facility (KNMFi), Karlsruhe Institute of Technology (KIT), Hermann-von-Helmholtz-Platz 1 76344 Eggenstein-Leopoldshafen, Germany
[c] Université Paris Est, ICMPE (UMR 7182), CNRS, UPEC, 2-8, Rue H. Dunant F-94320, Thiais, France
[d] Institute for Materials (IM), Ruhr University Bochum (RUB), Universitätsstr. 150 44780 Bochum, Germany

ARTICLE INFO

Keywords:
Refractory high entropy alloys
B2 precipitates
Coarsening
Ripening

ABSTRACT

The mechanical behavior of precipitation-strengthened materials is strongly influenced by precipitate morphological characteristics and lattice misfit to the matrix. This study examines the impact of 1 at. % Zr on thermal stability and coarsening kinetics in a refractory high-entropy A2-B2 alloy with the composition 27.3Ta-27.3Mo-27.3Ti-8Cr-10Al (at. %). We demonstrate that this minor Zr addition does not lead to the formation of other intermetallic phases, while the Zr strongly partitions into the B2 phase and induces a pronounced change in the precipitate morphology from cuboidal/elongated to spherical, accompanied by an increased number density. Despite coarsening close to the precipitate solvus temperature, extremely slow coarsening kinetics compared to other alloy systems is obtained mainly attributed to much higher solidus temperature rather than misfit or precipitate morphology alone. Overall, this work underscores the potential of tailoring precipitate characteristics to potentially enhance microstructural stability of B2 precipitates and creep resistance in advanced body centered cubic (BCC) superalloys.

Manuscript

The advancement of high-temperature structural (metallic) materials, most notably superalloys, depends on the precise control of matrix-precipitate misfit and precipitate morphology [1–5]. Alloying elements play a crucial role in tailoring these microstructural features, which in turn significantly influence the mechanical properties, particularly the creep resistance [6,7]. Spherical precipitates are often reported to result in good thermal stability and slow coarsening kinetics due to only a small lattice mismatch contributing to elastic strain energy [8–10].

Research on Ni- and Co-based superalloys showed that the matrix-precipitates lattice misfit can be tuned by alloying, affecting precipitate morphology. In Ni-based alloys (with A1-$L1_2$ two-phase microstructure $(\gamma - \gamma')$, Al, Ti, Ta, and Nb favor the formation of coherent $L1_2$, while Re and W enhance solid solution strengthening of the A1 matrix [11]. In emerging BCC superalloys, including Cr-, W- or Fe-based systems, elements like Al, Ti, and Ta are often used to form strengthening B2 or $L2_1$ precipitates [12–16].

While the change in lattice misfit and precipitate morphology with micro-alloying is well documented in A1-$L1_2$ systems [17], similar studies in A2-B2 refractory high entropy alloys (RHEA) are missing. Recently, 27.3Ta-27.3Mo-27.3Ti-8Cr-10Al (at. %, TMT-8Cr-10Al) was reported exhibiting an A2–B2 microstructure. Its B2 phase is stable up to 1060 to 1070 °C and forms by a nucleation and growth mechanism. It has a slight positive relative difference of lattice parameters δ of (+ 0.6 ± 0.4) % (constraint condition) [18]. This relative difference in lattice parameters is expressed by:

$$\delta = \frac{2(a_{B2} - a_{A2})}{a_{B2} + a_{A2}} \quad (1)$$

Where a_{A2} and a_{B2} represent the lattice parameters of A2 and B2,

* Corresponding authors'.
E-mail addresses: raja.vikram@partner.kit.edu (R.J. Vikram), sandipan.sen@kit.edu (S. Sen), alexander.kauffmann@rub.de (A. Kauffmann), martin.heilmaier@kit.edu (M. Heilmaier).

https://doi.org/10.1016/j.scriptamat.2025.117026
Received 14 July 2025; Received in revised form 25 September 2025; Accepted 29 September 2025
Available online 4 October 2025

respectively. It is worth mentioning that a critical misfit (unconstrained condition) of $\delta \approx 0.4$ % has been identified in Ni-based superalloys above which misfit strain significantly influences the $L1_2$ precipitate coarsening kinetics and microstructural evolution [19].

Studies on Cr-based superalloys (A2–B2 microstructure; $\delta \approx 0.1$ %) have demonstrated lower coarsening rates (10^2 nm^3/h at 1000 °C) than those observed in Fe-, Co-, and Ni-based superalloys. The coarsening kinetics suggest low A2/B2 interfacial energies of around 40 mJ/m^2 at 1000 °C and are primarily attributed to the limited solubility of Ni and Al in the Cr matrix [6].

Thermal stability in TMT-8Cr-10Al might be further improved if δ is reduced closer to zero, an outcome achievable through microalloying. The B2 precipitates were found to be rich in Al and Ti, while the A2 matrix was enriched in Mo and Ta with Cr being equally distributed in both phases. Studies on $Al_{0.5}NbTa_{0.8}Ti_{1.5}V_{0.2}Zr$ [20] have revealed the presence of a B2-ordered phase primarily composed of Ti, Al, and Zr. However, the A2–B2 microstructure in this alloy is thermally unstable due to the formation of ω phase precipitates during prolonged annealing [21]. Given that the B2 phase in the TMT-8Cr-10Al is also rich in Ti and Al, 1 at. % Zr was chosen as alloying addition to target the B2 phase. Thus, the final composition of the new alloy investigated in this study is 27Ta-27Mo-27Ti-8Cr-10Al-1Zr (TMT-8Cr-10Al-1Zr).

Both alloys (TMT-8Cr-10Al and TMT-8Cr-10Al-1Zr) were synthesized using an Edmund Bühler GmbH AM/0.5 arc melting furnace under an Ar atmosphere. High-purity elements (Ta, Cr, Al and Zr 99.9 %, Mo 99.95 %, Ti 99.8 %) were sourced from chemPUR GmbH, Germany. 100 g buttons were produced. Subsequently, the as-cast TMT-8Cr-10Al-1Zr alloy was wrapped in Mo foil for homogenization at 1600 °C for 20 h to remove the as-cast dendritic microstructure. Details are described elsewhere [18,22]. The overall compositions of both TMT-8Cr-10Al [18] and TMT-8Cr-10Al-1Zr are shown in **Table S1** (see supplementary material, as determined via scanning electron microscopy energy-dispersive X-ray spectroscopy (SEM-EDS) and atom probe tomography (APT)) which confirm that there was no significant deviation from the targeted compositions. The addition of 1 at. % Zr did not result in notable changes to the overall alloy composition beyond the intended substitution.

To investigate the microstructure, samples were cut from the buttons using electrical discharge machining. A standard metallographic procedure was applied [18,22] and SEM was performed using a Zeiss LEO 1530 (Zeiss, Germany) operated at an acceleration voltage of 20 kV. Electron backscatter diffraction (SEM-EBSD) analysis was carried out using an EDAX Digiview system (Ametek, USA) integrated into a Zeiss Auriga 60 (Zeiss, Germany) to examine local crystallographic orientations and identify secondary phases. Differential scanning calorimetry (DSC) measurements were carried out for TMT-8Cr-10Al-1Zr to investigate the heat signatures of the ordering and precipitation reactions and to compare them to TMT-8Cr-10Al. Details are provided in [18,22,23]. CALPHAD calculations using Pandat software (CompuTherm LLC) with the RHEA database were employed to determine solidus temperatures using the nominal alloy compositions. These allow for the determination of homologous temperatures $T_{hom} = T/T_{solidus}$ across different alloys.

To evaluate thermal stability and aging kinetics, homogenized specimens underwent solution heat treatment at 1200 °C for 1 h followed by rapid water quenching. However, water quenching does not prevent the formation of small clusters of about 1 nm size as previously shown by Laube et al [22,23]. These clusters are the initial condition for the present coarsening study. Given the minimal compositional deviation, we expect similar cluster dimensions in the TMT-8Cr-10Al-1Zr alloy. These samples were then subjected to isothermal aging at 1000 °C for durations reaching 1000 h to systematically study microstructural evolution over extended timeframes. The samples were wrapped in a Ta foil and sealed in Ar-filled fused silica tubes to prevent oxidation.

Quantitative image analysis was conducted using ImageJ [24] on high-resolution SEM micrographs to evaluate the morphology and distribution of the B2 phase. The procedures for image segmentation and the parameters used for analyzing precipitate distribution [25] are provided in the supplementary material.

APT samples were prepared in a Strata 400 focus ion beam/scanning electron microscopy dual-beam device (Thermo Fisher Scientific, Waltham, MA, USA) using the lift-out method [26]. APT analysis was performed with a LEAP 4000X HR instrument (Cameca Instruments, Madison, WI, USA) at 50 K, at a detection rate of 0.5 %, and with a laser wavelength of 355 nm with a pulse energy of 40 pJ and pulse rate of 125 kHz. The APT reconstruction and data evaluation was performed with AP Suite 6.3 (Cameca Instruments).

To assess the aspect of brittleness or plastic deformability in the A2–B2 multiphase alloy system, microindentation tests were conducted using a Qness Q10+ microhardness tester under loads of HV1–HV5 to generate intense localized plastic deformation regions.

The XRD pattern of TMT-8Cr-10Al-1Zr (see supplementary material) after homogenization and slow cooling suggests only A2 crystal structure being present like for the Zr-free alloy. However, A2 and B2 cannot be properly differentiated by lab-based XRD in these alloys [27]. Thus, microstructural investigations of Zr-free TMT-8Cr-10Al quenched after long-term annealing at various temperatures were conducted and revealed the solvus temperature T_{solvus} of a precipitate phase between 1060 and 1070 °C [18]. The B2 ordering of the precipitates during cooling occurs close but at a slightly lower temperature of at 1055 °C as obtained by DSC measurements [22,23]. The temperature dependence of the enthalpy derivative dH/dT of TMT-8Cr-10Al-1Zr for different heating rates is shown in Fig. 1a. The extrapolated peak temperature indicating the ordering temperature of the precipitates is 1056 °C. Within the accuracy of the temperature measurement and extrapolation, this is the same as for the Zr-free alloy [22]. Inverse pole figure (IPF) mapping from SEM-EBSD shows equiaxed grains with a size exceeding 200 μm in diameter and random crystallographic orientations (Fig. 1b). The homogenized microstructure of the alloy is represented in Fig. 1c. High-magnification backscattered electron (SEM-BSE) micrographs reveal fine B2 precipitates dispersed throughout the A2 matrix and formed during furnace cooling (Fig. 1d). For TMT-8Cr-10Al-1Zr, the precipitate size in this condition was (4.0 ± 2.2) nm in radius indicating that existing clusters lower the nucleation barrier, leading to diffusion-controlled coarsening and a stable precipitate distribution.

As no relevant differences in microstructural appearance, ordering temperature and chemical constitution (except for Zr, revealed by APT in the following, see supplementary material **Table S1**) are obtained, the T_{solvus} is assumed to be similar to the Zr-fee alloy between 1060 and 1070 °C. The phase stabilities seem similar between the alloys.

A coarsening study was conducted at 1000 °C for durations of 10, 100, and 1000 h for both alloys. As illustrated in Fig. 2a-f, the TMT-8Cr-10Al-1Zr retains spherical precipitates with minimal coarsening over time (Fig. 2d-f). By contrast, the TMT-8Cr-10Al undergoes directional coarsening leading to elongated precipitates due to its positive δ between the precipitate and matrix [1,18]. The spherical precipitate shape in TMT-8Cr-10Al-1Zr strongly suggests a near zero δ [28]. This morphological stability is likely to enhance the high-temperature mechanical properties, particularly the creep resistance [29,30]. It is important to note that even small variations in temperature or minor alloying additions can alter the misfit by several tenths of a percent [31,32], thereby significantly influencing coarsening behavior. The suppression of directional coarsening despite identical ageing conditions of both alloys and only marginally changed base compositions of the constituting phases (see supplementary material **Table S1**) strongly suggests a reduced elastic driving force. In the present status of research, most thermo-elastic properties required for a detailed quantification of this effect are unknown. Thus, the quantification is beyond the scope of the present study.

Table 1 shows the coarsening kinetics revealing distinct differences between the alloys. Zr-free TMT-8Cr-10Al exhibits systematically larger equivalent diameters across all aging durations, paired with a slightly lower precipitate area fraction after 1000 h at 1000 °C. After 10 h aging,

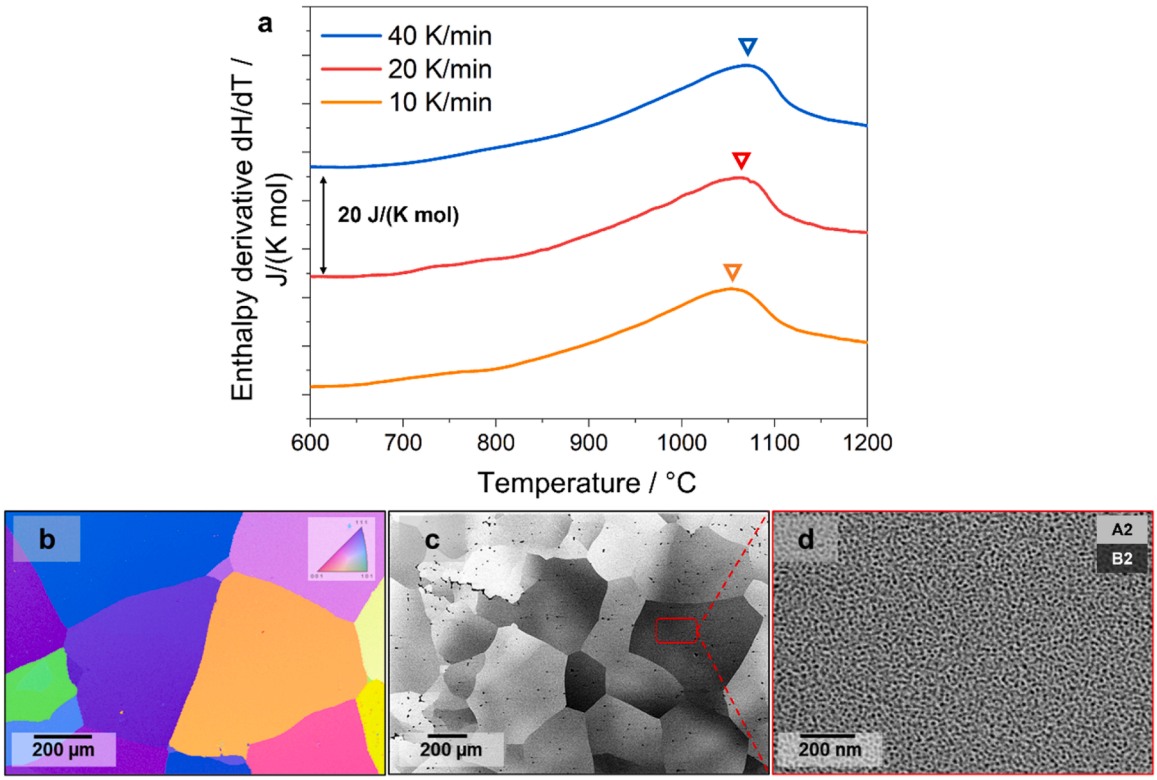

Fig. 1. Characterization of homogenized **TMT-8Cr-10Al-1Zr**: (a) DSC results with varying heating rates, (b) SEM-EBSD IPF map revealing equiaxed grains with random crystallographic texture. SEM-BSE mode at increasing magnifications, illustrating the microstructure after homogenization and slow cooling: (c) low magnification overview (orientation contrast) showing grains with sizes exceeding 200 µm, (d) high magnification detail (*Z* contrast) highlighting evenly distributed spherical B2 precipitates.

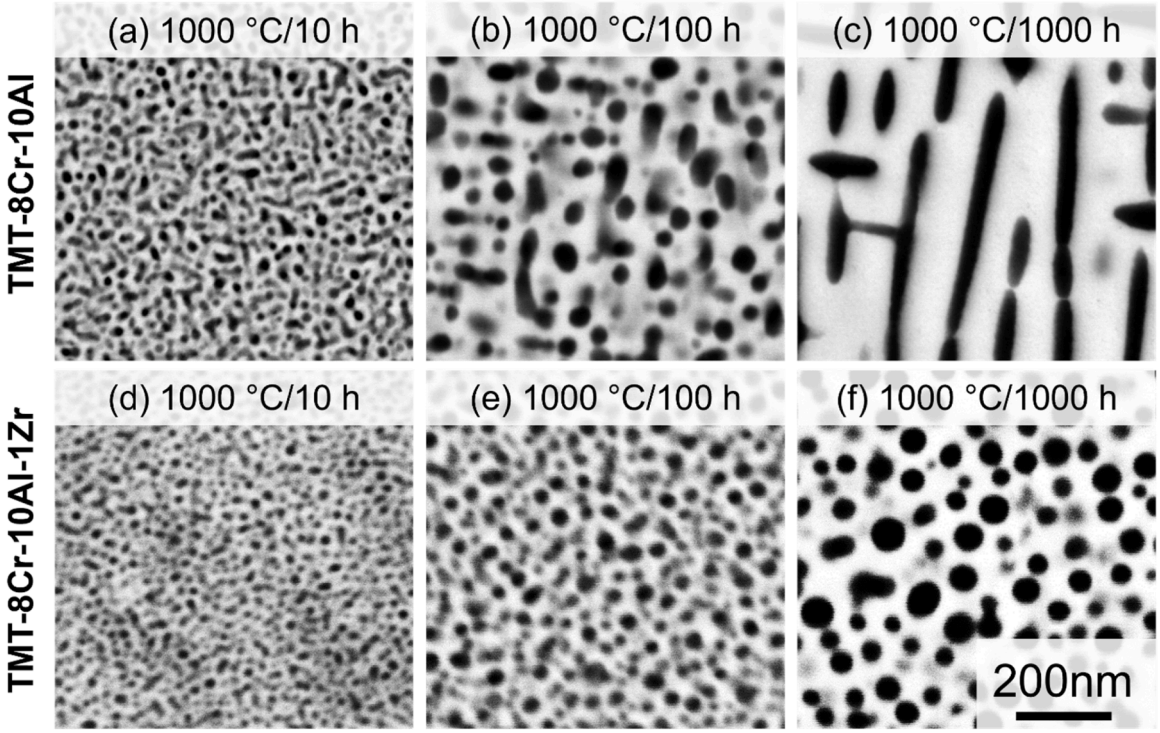

Fig. 2. Evolution of microstructure in (a-c) **TMT-8Cr-10Al**, and (d-f) and **TMT-8Cr-10Al-1Zr**, both aged at 1000 °C for 10, 100 and 1000 h. SEM-BSE micrographs (*Z* contrast) illustrating the distribution and morphology of B2 precipitates in the A2 matrix. Note the distinct differences in precipitate shape and size distribution between the Zr-free and Zr-containing alloys across different ageing durations.

Table 1
Comparative analysis of microstructural features in TMT-8Cr-10Al and TMT-8Cr-10Al-1Zr at 1000 °C. Please refer to supplementary material to more detailing of the parameters.

Parameters	TMT-8Cr-10Al				TMT-8Cr-10Al-1Zr			
Time / h	10	100	200	1000	10	100	200	1000
Actual mean radius $\bar{r}_{act}$ / nm	22 ± 7	36 ± 10	36 ± 14	55 ± 6	9 ± 4	18 ± 6	24 ± 9	36 ± 15
Area % B2	29 ± 2	29 ± 1	26 ± 2	26 ± 3	29 ± 3	29 ± 2	27 ± 2	28 ± 1
Mean Center-to-center particle spacing L / nm	40 ± 3	62 ± 3	75 ± 5	122 ± 7	25 ± 2	48 ± 4	65 ± 3	107 ± 4
Circularity index	0.63 ± 0.21	0.71 ± 0.15	0.60 ± 0.12	0.49 ± 0.20	0.68 ± 0.18	0.85 ± 0.13	0.84 ± 0.11	0.82 ± 0.12
Aspect ratio	1.70 ± 0.65	1.74 ± 0.52	1.61 ± 0.48	3.33 ± 2.22	1.29 ± 0.21	1.49 ± 0.11	1.48 ± 0.12	1.45 ± 0.21
Number density N_V / 10^3 μm^3	58	19	9.4	3.6	310	40	14	4.1

TMT-8Cr-10Al-1Zr showed an order-of-magnitude higher precipitate number density demonstrating enhanced nucleation. The B2 precipitate fraction (Table 1) remains constant within the standard deviation for both alloys but shows a slight deviation from CALPHAD-based lever rule predictions (see supplementary material Table S2), likely due to consumption of B2 phase formed at grain boundaries. The evolution of the circularity index (CI) and aspect ratio (AR) given by the ratio of major axis (b) and minor axis (a) confirms the visual observation of shape stability in TMT-8Cr-10Al-1Zr. These shape descriptors also capture the anisotropic nature of elongated precipitates. In addition, the equivalent diameter was calculated from the b,a for the elongated precipitates to quantitatively address anisotropy (see Section 4 of supplementary material for details). Zr addition reduces δ and internal stresses as the primary drivers of directional coarsening. Thereby, coarsening is decelerated as well [32,33].

In A2–B2 alloys, an elastic contrast of B2 relative to A2, together with lattice misfit, contributes to anisotropic coarsening or rafting. The N-type rafting during creep (elongation perpendicular to the compression loading axis) obtained by Yang et al [18] suggests a positive misfit and higher elastic stiffness of B2 particles. In the present alloys, the A2 and B2 compositions are almost the same, but 1 at. % Zr partitions preferentially into B2, potentially altering its lattice parameter or elastic constants. This can reduce lattice misfit and thereby the elastic driving force for rafting. The absence of rafting in the Zr-containing alloy is consistent with a near-zero misfit scenario. However, precise quantification of the thermo-elastic behavior of the constituting phases is required.

APT analysis on TMT-8Cr-10Al-1Zr aged at 1000 °C for 100 h was performed to investigate the partitioning behavior between matrix and precipitates. The Ta isosurfaces in the 3D reconstruction in Fig. 3a reveal the B2 precipitates. 1D-concentration profiles were generated across an A2/B2 interface to quantify the elemental distribution, Fig. 3b These profiles indicate a strong Zr partitioning into the B2 phase. Fig. 3c shows a magnified region highlighting Al, Cr and Zr concentration profiles from Fig. 3b Like for TMT-8Cr-10Al [22,23], the B2 precipitates in TMT-8Cr-10Al-1Zr are also enriched in Ti and Al in addition to Zr. The

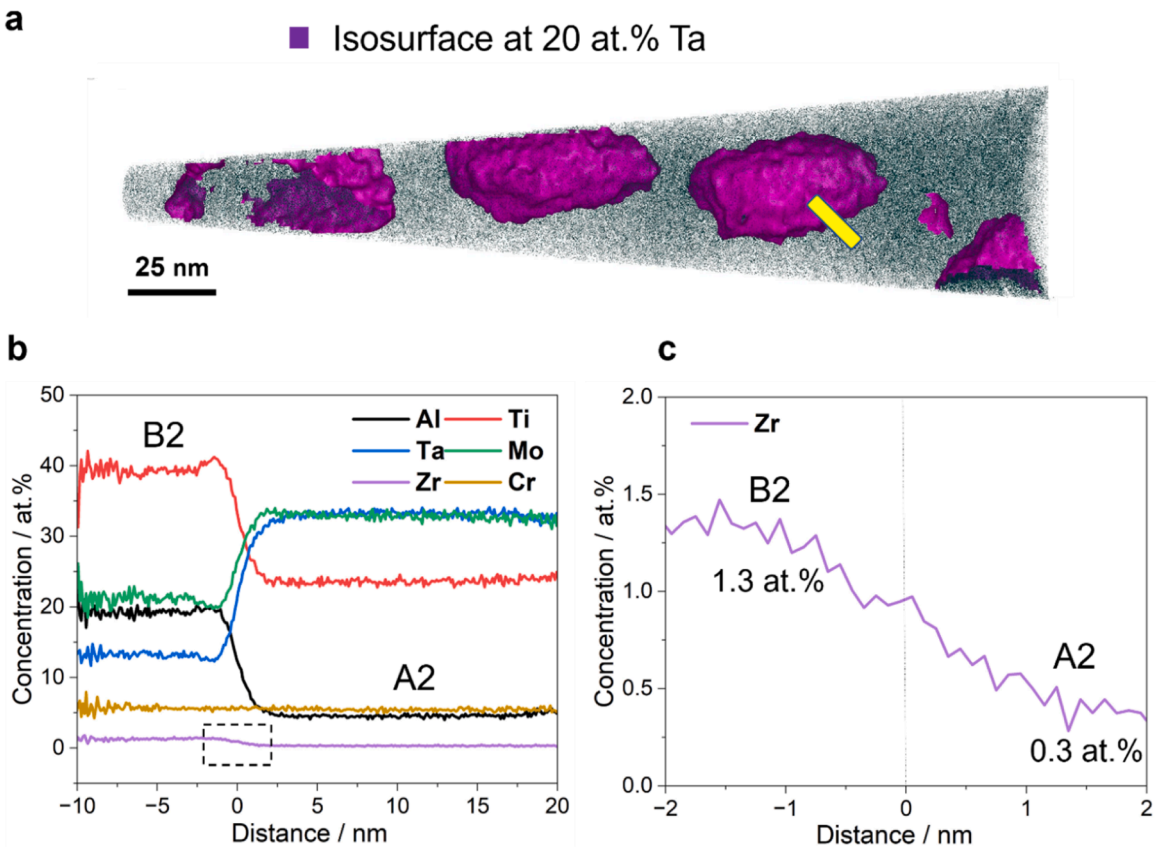

Fig. 3. APT analysis of the A2–B2 microstructure in TMT-8Cr-10Al-1Zr. (a) 3D reconstruction showing Ta isosurface (pink) in the analyzed volume. (b) Proximity histograms across the A2/B2 interface for the two central precipitates shown in (a) and (c) magnified concentration profile highlighting Zr concentration at the A2/B2 interface.

A2 matrix is likewise enriched in Ta and Mo while being depleted in Zr. Cr is uniformly distributed. Table 2 presents the chemical composition of the elements in the two phases (in at. %) for both alloys. The Ti/Al and Ti/Mo ratios approach 2 suggesting that the B2 phase resembles Ti(Al, Mo) [33,34].

The coarsening behavior and morphology of the precipitates are determined by the interplay between minimizing the misfit strain energy and interfacial energy [35,36]. The spherical precipitate morphology in TMT-8Cr-10Al-1Zr indicates the dominance of interfacial energy over misfit strain energy [37,38]. Although the morphology of the precipitates remains quite stable, the coarsening rates are important to quantify by using:

$$\bar{r}_{\mathrm{act}}^{n} - \bar{r}_{0}^{n} = \kappa\, t \tag{2}$$

$\bar{r}_0$ is the radius after completion of the precipitation reaction, $\bar{r}_{\mathrm{act}}$ the mean actual precipitate radius (see Section 4 of supplementary material) after different aging times t and κ the coarsening rate constant. The power-law exponent n is time-independent, if the coarsening mechanism remains unchanged. $n = 3$ is obtained for bulk diffusion-controlled coarsening [39]. Based on the Lifshitz-Slyozov-Wagner theory [40], κ can be approximated in a multicomponent system as [39,41]:

$$\kappa = \frac{8\gamma\, V_{\mathrm{m}}^{\mathrm{B2}}\, D_i^{\mathrm{A2}}}{9R\, T \sum_i^N \left(c_i^{\mathrm{B2}} - c_i^{\mathrm{A2}}\right)^2 \Big/ c_i^{\mathrm{A2}}} \tag{3}$$

γ is the interfacial energy, $V_{\mathrm{m}}^{\mathrm{B2}}$ the molar volume of B2 precipitate, R the gas constant, T the absolute temperature, c_i^j and D_i^j the concentration and diffusion coefficient of i in phase j [33].

Fig. 4a shows the variation of $\bar{r}_{\mathrm{act}}^3$ with respect to t. The κ for TMT-8Cr-10Al-1Zr is very small with (48 ± 4) nm^3/h at 1000 °C. Such a low κ is highlighted when compared to TMT-8Cr-10Al with (77 ± 4) nm^3/h. However, as the coarsening of TMT-8Cr-10Al occurs directionally, a more realistic prolate spheroid might be used to properly describe the precipitates' shape change over time. Considering this anisotropy, κ is evaluated to even (158 ± 18) nm^3/h. While this is larger than for TMT-8Cr-10Al-1Zr, it is still smaller than that observed in other alloys (see Table 2). The data are compared to newly developed Ni-based (A1–L1$_2$) and Cr-based superalloys (A2–B2) in Fig. 4b It can be clearly inferred that TMT-8Cr-10Al-1Zr exhibits slower coarsening kinetics at much higher T/T_{solvus} as compared to other superalloys. A controlled and slow coarsening behavior is useful as it preserves a fine spatial distribution of precipitates over prolonged exposure, which can be beneficial for maintaining creep resistance. Thus, slower coarsening rates are desirable to retain strengthening phases and delay degradation in mechanical properties.

When the coarsening kinetics are plotted against the homologous temperature T/T_{solidus} (Fig. 4c), the TMT-8Cr-10Al/−1Zr alloys exhibit lower κ at lower homologous temperature compared to Ni- and Cr-based superalloys. Thus, a promising design strategy to improve coarsening kinetics is to engineer alloys with an elevated solidus temperature as in the present study. Such alloys exhibit lower intrinsic diffusivities of their constituent elements at a given operating temperature. This in turn suppresses precipitate coarsening, thereby enhancing thermal stability without compromising microstructural integrity. However, the operating temperature is inherently limited by the precipitate solvus temperature, a constraint that fundamentally restricts mechanical performance of precipitation-strengthened alloys.

κ is influenced by four key factors: the interfacial energy γ, molar volume V_{m}, diffusivity D of the constituent species, and the concentration gradient $\Delta C_{\mathrm{i}} = \left(c_i^{\mathrm{B2}} - c_i^{\mathrm{A2}}\right)^2 / c_i^{\mathrm{A2}}$ of the constituent species between the matrix and precipitates. κ is directly proportional to γ, V_{m} and D while being inversely proportional to the squared relative concentration difference ΔC_{i}.

When comparing the coarsening behavior of TMT-8Cr-10Al and TMT-8Cr-10Al-1Zr, the similarities in composition suggest that D and V_{m} are likely comparable. The concentration gradient ΔC_i in TMT-8Cr-10Al and TMT-8Cr-10Al-1Zr is relatively small for Ta, Mo and Ti, but more significant for Al, see Table 2. However, in complex multicomponent alloys, it is generally accepted that the coarsening kinetics—specifically the evolution of average radius and number density—are primarily controlled by the species with lowest diffusivity [42,43]. Since the difference in ΔC_i for Ta and Mo is minor in both alloys, their contributions to κ are expected to be similar. Consequently, any difference in κ between these two alloys is likely attributed to variations in the interfacial energy γ. The latter typically comprises a chemical contribution γ_{ch} and an elastic strain contribution γ_{el} [44]. The elastic component γ_{el} is directly proportional to the square of the lattice misfit δ^2. For TMT-8Cr-10Al, δ is approximately +0.6 % (in constraint condition), whereas it is close to 0 for TMT-8Cr-10Al-1Zr. As a result, γ_{el} and the total interfacial energy γ is expected to be higher in TMT-8Cr-10Al.

Table 2
Composition of A2 (matrix) and B2 (precipitate) phases analyzed via APT in the current TMT-8Cr-10Al(+1Zr) alloy and reference A2–B2/A1–L1$_2$ systems, measured at 900–1000 °C for κ parameter analysis. Data highlight important contributing parameter influencing kinetic coarsening behavior.

	Ta-Mo-Ti - Base	Phase	Composition (at. %)						T / °C	κ / nm^3/h
			Ta	Mo	Ti	Cr	Al	Zr		
BCC	TMT-8Cr-10Al-1Zr	**A2**	32.9 ± 0.3	33.3 ± 0.2	23.5 ± 0	5.4 ± 0.1	4.5 ± 0	0.3 ± 0	**1000**	**48 ± 4**
		B2	13.1 ± 0.2	21.1 ± 0.3	39.5 ± 0	5.7 ± 0.3	19.2 ± 0.2	1.3 ± 0.1		
		ΔC_i	**12**	**5**	**12**	**0**	**48**	**3**		
	TMT-8Cr-10Al	**A2**	30.4 ± 0.3	31.5 ± 0.2	25.0 ± 0	7.0 ± 0.1	5.7 ± 0	–	**1000**	**158 ± 18**
		B2	14.8 ± 0.2	21.7 ± 0.3	38.4 ± 0	6.6 ± 0.3	18.2 ± 0.2	–		
		ΔC_i	**8**	**3**	**7**	**0**	**27**	**–**		

	Cr - Base	**Phase**	**Composition (at. %)**					
			Cr	**Ni**	**Al**	**Fe**		
	Cr-5Ni-5Al	**A2**	98.7 ± 0.1	0.3 ± 0.1	0.9 ± 0.1	–	**1000**	**222** [6]
		B2	0.9 ± 0.3	52.7 ± 0.5	46.4 ± 0.5	–		
		ΔC_i	**96**	**9152**	**2300**	**–**		
	Cr-5Ni-5Al-10Fe	**A2**	86.1 ± 0.3	1.2 ± 0.1	1.4	11.2 ± 0.3	**1000**	**914** [6]
		B2	0.9 ± 0.2	51.2 ± 0.3	44.1 ± 0.2	3.7 ± 0.1		
		ΔC_i	**84**	**2083**	**1302**	**5**		

	Ni - Base	**Phase**	**Nominal composition (at. %)**					
			Ni,Co	**Al,Ti**	**Ta,Cr**	**Mo,W**		
FCC Superalloys	CMSX2	**A1–L1$_2$ (at. %)**	66.4, 4.6	5.6, 1.0	6.0, 7.8	0.6, 7.9	**1000**	**216,000** [46]
	IN939	**A1–L1$_2$ (at. %)**	46.2, 18.4	4.1, 4.3	0.4, 24.3	0, 0.6	**910**	**17,642** [47]

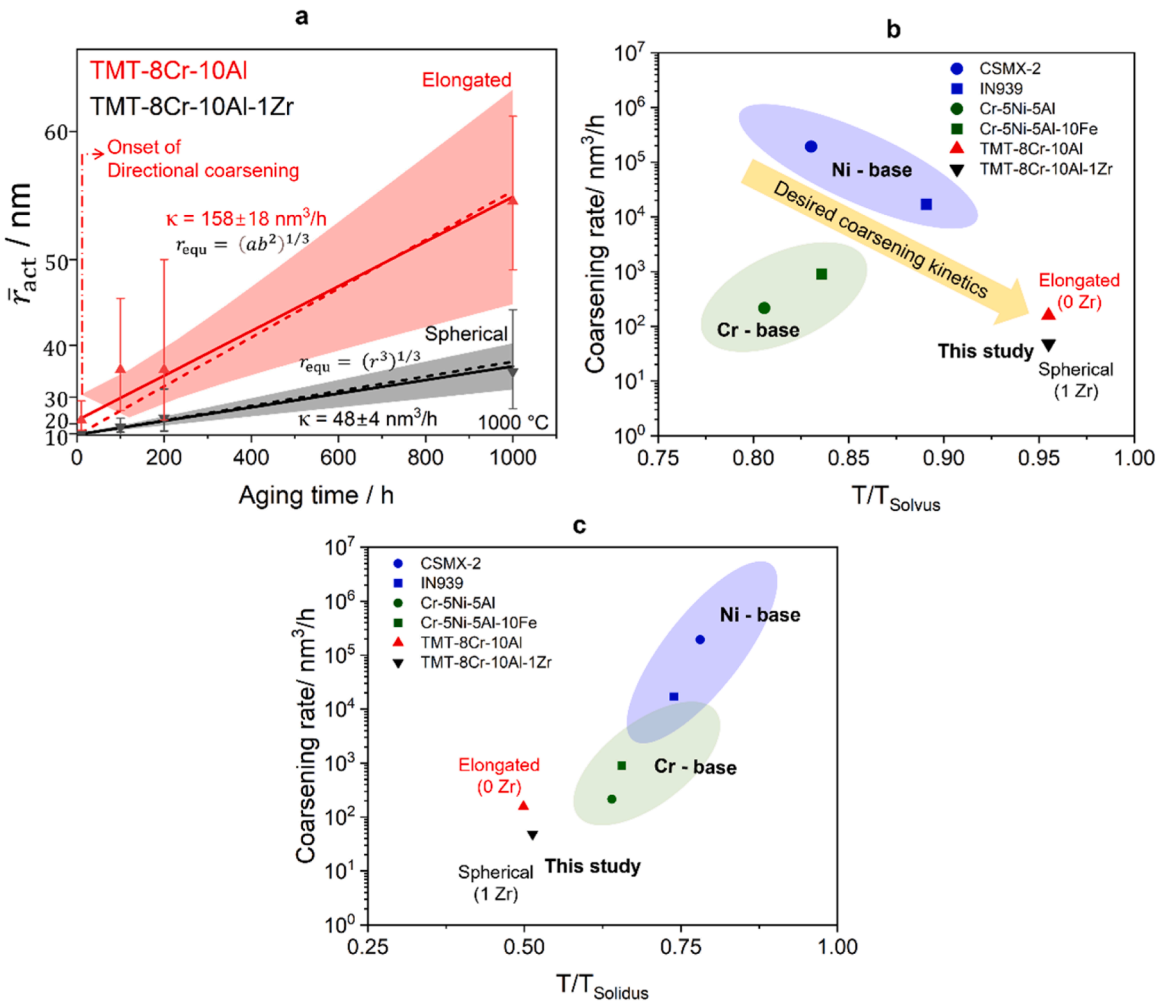

Fig. 4. (a) Plot of $\bar{r}^3_{act}$ vs. ageing time for determining the coarsening rate. $\bar{r}_{act}$ is used for clarity and physical interpretation; fitting parameters and the role of r_o are detailed in the Supplementary Information. Coarsening rate as a function of ageing temperature for ferritic, Ni-, and Cr-based superalloys [6], normalized to their (b) respective precipitate solvus temperatures T_{solvus} and (c) solidus temperatures $T_{solidus}$ (see supplementary material **Table S3**).

This higher γ (factor of 1.5) leads to a higher κ (factor of 1.5), consistent with experimental observations.

When comparing κ across different alloy systems, the analysis becomes more complex. In this discussion, we consider two A2–B2 alloy systems, TMT-8Cr-10Al/−1Zr (*Ta-Mo-Ti alloys*) and Cr-5Ni-5Al/Cr-5Ni-5Al-10Fe (*Cr-Ni-Al alloys*). For both systems, the lattice misfit can be assumed to be comparable due to the presence of stable spherical precipitates, suggesting a similar contribution of the interfacial energy γ to κ. However, the other three parameters influencing κ, namely V_m, D, and ΔC_i likely differ significantly. Based on data from Table 2, ΔC_i is higher in the Cr-Ni-Al alloys than in Ta-Mo-Ti alloys. Additionally, due to the presence of elements with larger atomic radii such as Ta and Mo, V_m of the B2 precipitates in the Ta-Mo-Ti alloys is expected to be larger than in the Cr-Ni-Al alloys. This combination of a higher V_m and lower ΔC_i in the Ta-Mo-Ti alloys would suggest higher κ for this system. However, experimental measurements at 1000 °C indicate the opposite. This discrepancy is most likely attributed to the diffusivity D as the rate-determining factor. While accurate determination of diffusivities in such multicomponent A2–B2 systems is challenging, a qualitative understanding can be obtained by considering the diffusivities of the constituent elements at 1000 °C.

According to the thermodynamical calculations, $T_{solidus}$ are 2210 °C and 2282 °C for TMT-8Cr-10Al and TMT-8Cr-10Al, respectively, while it is only 1710 °C for the Cr-5Ni-5Al. Thus, the homologous temperatures T_{hom} at 1000 °C are 0.51 and 0.64 for TMT-8Cr-10Al and Cr-5Ni-5Al, respectively. These findings indicate that the diffusivities of the constituent elements may be much faster in Cr-Ni-Al alloys, which rationalizes the smaller κ in the Ta-Mo-Ti alloys. This is in line with experimental reports showing that the diffusivity of Zr in other BCC refractory high entropy alloys increased by two orders of magnitude when the homologous temperature is raised from 0.51 to 0.64 [45]. This simple qualitative analysis leads to conclude that the diffusivity in the A2–B2 alloys is the rate-determining factor for κ over the other parameters. The comparison of the BCC and FCC superalloy systems is of engineering interest. However, a detailed assessment of the individual parameters is not meaningful due to even more assumptions being required.

The resembled Ti(Al,Mo)-type B2 [48,49] phase as well as the similar Ti(Al,Nb) [49–51] are known to exhibit appreciable ductility during room temperature deformation. Further, Gagneur et al [49] demonstrate an automated indentation-based slip-trace method that reveals the active slip systems in B2 intermetallics, providing new insights into their deformation mechanisms and pathways to improved ductility. The ductility in these B2 compounds has been attributed to the possible activation of <111>{112} and <111>{011} slip systems owing to its relatively low antiphase boundary (APB) energy [50,52,53]. Additionally, the combination with the extremely small size of the precipitates and a low δ might allow for slip transfer through the B2 phase [54]. More recently, it has been observed that BCC superalloys exhibit δ ranging from nearly zero up to about 8 % indicating the role of misfit in tailoring

microstructural stability and creep resistance [32]. Overall, despite the difference in alloying element (Mo versus Nb), the B2 phases in both systems are expected to deform via similar mechanisms under ambient conditions, resulting in comparable ductile behavior. Simple indentation testing can effectively probe this response and enhance our understanding. Therefore, HV1 Vickers indentation was performed on TMT-8Cr-10Al-1Zr aged at 1000 °C for 1000 h (Fig. 5a). In regions of intense plastic localization, slip traces were observed. Near the indentation, interaction with B2 precipitates resulted in complete precipitate cutting (Fig. 5b) [41–43]. Interestingly, the observed behavior suggests that these coherent spherical precipitates have the potential to offer ductility in refractory A2+B2 superalloys at ambient temperature [50, 51]. The ability of dislocations to penetrate and transmit through the precipitates confirms their coherency even after prolonged high-temperature aging [52,54]. A similar approach applied to TMT-8Cr-10Al (Fig. 5c,d) shows that the elongated precipitates also undergo shearing, suggesting the coherent nature of the B2 precipitate even at a larger misfit. While shape often influences the dislocations-precipitate interaction, the observation of both elongated and spherical precipitate cutting suggests that the critical resolved shear stress required for cutting may be relatively low.

In conclusion, the refractory high entropy alloy 27.3Ta-27.3Mo-27.3Ti-8Cr-10Al-1Zr (at. %) with a two-phase, A2 matrix + B2 precipitate microstructure shows promising thermal stability at high temperatures:

1. Microalloying with Zr changes the lattice parameter difference between A2 and B2 to close to zero without forming any undesirable intermetallic phases.
2. Zr is enriched in the spherical, likely coherent B2 precipitates.
3. The precipitates exhibit exceptional stability against coarsening at 0.95 of their solvus temperature mainly due to a higher solidus temperature and, thus, slow diffusivity of Ta and Mo.
4. With respect to ductility of A2+B2 alloys, coherency and slip transfer from A2 to B2 is required which is revealed in the investigated alloys.

These findings open a promising avenue for designing advanced BCC superalloys with enhanced mechanical performance. To allow for targeted alloy design, the currently existing thermodynamic assessments and models need to be improved with respect to the type of B2 compounds formed, their ordering temperatures and the correct the positions of the miscibility gaps.

RJV, AK, MH would like to express their sincere gratitude to the Alexander von Humboldt Foundation for their generous funding, which has been pivotal in supporting the research. Their financial assistance enabled us to conduct essential experiments. LY is financially supported by China Scholarship Council (CSC) with No 202207000023. This work was partly carried out with the support of the Karlsruhe Nano Micro Facility (KNMFi, www.knmf.kit.edu, proposal number 2024–033–032157), a Helmholtz Research Infrastructure at Karlsruhe Institute of Technology (KIT, www.kit.edu).

The data presented in this study are available at zenodo via https://doi.org/10.5281/zenodo.17014208 under CC BY-SA 4.0 license. Further information is available upon request with alexander.kauffmann@rub.de.

We confirm that this manuscript has not been published previously by any of the authors and is not under consideration for publication in another journal.

CRediT authorship contribution statement

R.J. Vikram: Writing – review & editing, Writing – original draft,

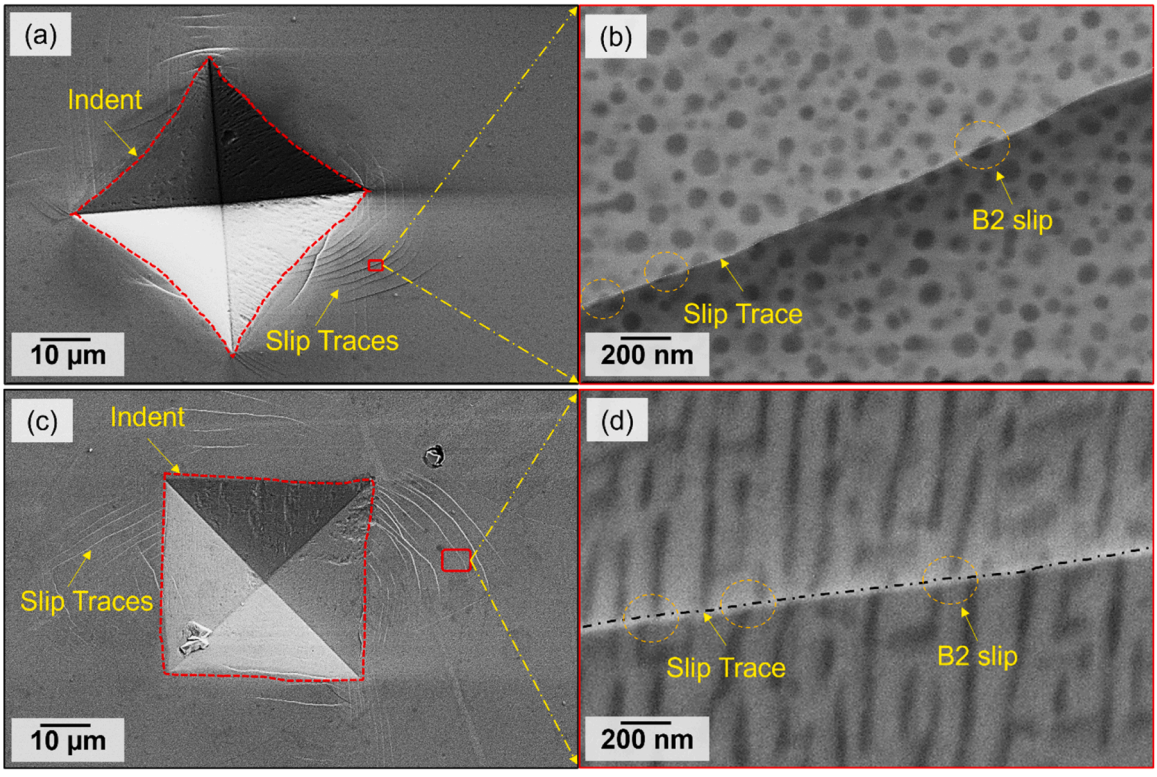

Fig. 5. Deformation characteristics of B2 precipitates in A2 matrix in a Zr-containing specimen aged at 1000 °C for 1000 h. Vickers indentation (HV1 load) showing intense localized plastic deformation with prominent slip traces for (a) TMT-8Cr-10Al-1Zr and (c) TMT-8Cr-10Al with hardness of (674 ± 9) and (670 ± 13) HV, respectively. High-magnification SE micrographs revealing B2 nanoprecipitates (encircled) cut along the slip direction for (b) TMT-8Cr-10Al-1Zr and (d) TMT-8Cr-10Al. The complete cutting mechanism confirms coherent interfacial matching between B2 precipitates and A2 matrix.

Visualization, Validation, Project administration, Methodology, Investigation, Formal analysis, Data curation, Conceptualization. **Sandipan Sen:** Writing – review & editing, Visualization, Methodology, Investigation, Formal analysis, Data curation, Conceptualization. **Liu Yang:** Writing – review & editing, Visualization, Validation, Software, Methodology, Investigation, Formal analysis, Data curation. **Michael K. Eusterholz:** Software, Methodology, Investigation, Formal analysis, Data curation. **Amin Radi:** Writing – review & editing, Investigation. **Daniel Schliephake:** Writing – review & editing, Validation, Investigation, Formal analysis. **Jean-Philippe Couzinié:** Writing – review & editing, Validation, Investigation, Formal analysis. **Alexander Kauffmann:** Writing – review & editing, Supervision, Resources, Investigation, Funding acquisition, Formal analysis, Data curation, Conceptualization. **Martin Heilmaier:** Writing – review & editing, Supervision, Resources, Investigation, Funding acquisition, Conceptualization.

Declaration of competing interest

The authors declare that they have no known competing financial interests or personal relationships that could have appeared to influence the work reported in this paper.

Supplementary materials

Supplementary material associated with this article can be found, in the online version, at doi:10.1016/j.scriptamat.2025.117026.

References

[1] H. Mughrabi, U. Tetzlaff, Microstructure and high-temperature strength of monocrystalline nickel-base superalloys, Adv. Eng. Mat. 2 (2000) 319–326.
[2] J. Zhang, F. Lu, T. Huang, R. Li, G. Zhang, L. Liu, An advanced approach to improve the high-temperature property for Ni-based superalloys: interface segregation manipulation, Mat. Sci. Eng. A. 881 (2023) 145382.
[3] D.B. Miracle, O.N. Senkov, A critical review of high entropy alloys and related concepts, Acta. Mater. 122 (2017) 448–511.
[4] D.B. Miracle, O.N. Senkov, C. Frey, S. Rao, T.M. Pollock, Strength vs temperature for refractory complex concentrated alloys (RCCAs): a critical comparison with refractory BCC elements and dilute alloys, Acta. Mater. 266 (2024) 119692.
[5] O.N. Senkov, G.B. Wilks, D.B. Miracle, C.P. Chuang, P.K. Liaw, Refractory high-entropy alloys, Intermetallics 18 (2010) 1758–1765.
[6] K. Ma, T. Blackburn, J.P. Magnussen, M. Kerbstadt, P.A. Ferreirós, T. Pinomaa, C. Hofer, D.G. Hopkinson, S.J. Day, P.A.J. Bagot, M.P. Moody, M.C. Galetz, A. J. Knowles, Chromium-based bcc-superalloys strengthened by iron supplements, Acta. Mater. 257 (2023) 119183.
[7] N. Parkes, R. Dodds, A. Watson, D. Dye, C. Hardie, S.A. Humphry-Baker, A. J. Knowles, Tungsten-based bcc-superalloys: thermal stability and ageing behaviour, Int. J. Refract. Met. 113 (2023) 106209.
[8] Y. Ma, B. Jiang, C. Li, Q. Wang, C. Dong, P.K. Liaw, F. Xu, L. Sun, The BCC/B2 morphologies in AlxNiCoFeCr high-entropy alloys, Metals. 7 (2017) 57.
[9] T.K. Tsao, A.C. Yeh, C.M. Kuo, K. Kakehi, H. Murakami, J.W. Yeh, S.R. Jian, The high temperature tensile and creep behaviors of high entropy superalloy, Sci. Rep. 7 (2017) 12658.
[10] C. Booth-Morrison, R.D. Noebe, D.N. Seidman, Effects of a tantalum addition on the morphological and compositional evolution of a model Ni-Al-Cr superalloy, in: C.R. Roger (Ed.), Superalloys 2008, 2008, pp. 73–79. TMS (The Minerals, Metals & Materials Society).
[11] Roger C. Reed, The superalloys: Fundamentals and Applications, Cambridge University Press, Cambridge, 2006.
[12] C. Frey, H. You, S. Kube, G.H. Balbus, K. Mullin, S. Oppenheimer, C.S. Holgate, T. M. Pollock, High temperature B2 precipitation in Ru-containing refractory multi-principal element alloys, Met. Mater. Trans. A. 55 (2024) 1739–1764.
[13] M.K. Moczadlo, E.A. Lass, Microstructure and phase equilibria in BCC-B2 Nb-Ti-Ru refractory superalloys, Metals 17 (2024) 5429.
[14] Z.T. Kloenne, J.P. Couzinié, M. Heczko, R. Gröger, G.B. Viswanathan, W.A.T. Clark, H.L. Fraser, On the bcc/B2 interface structure in a refractory high entropy alloy, Scr. Mater. 223 (2023) 115071.
[15] O.N. Senkov, B. Crossman, S.I. Rao, J.P. Couzinie, D.B. Miracle, T.M. Butler, R. Banerjee, M. Mills, Mechanical properties of an Al10Nb20Ta15Ti30V5Zr20 A2/B2 refractory superalloy and its constituent phases, Acta. Mater. 254 (2023) 119017.
[16] A.J. Knowles, D. Dye, R.J. Dodds, A. Watson, C.D. Hardie, S.A. Humphry-Baker, Tungsten-based bcc-superalloys, Appl. Mater. Today. 23 (2021) 101014.
[17] J.S. Van Sluytman, T.M. Pollock, Optimal precipitate shapes in nickel-base γ–γ′ alloys, Acta. Mater. 60 (2012) 1771–1783.
[18] L. Yang, S. Sen, D. Schliephake, R.J. Vikram, S. Laube, A. Pramanik, A. Chauhan, S. Neumeier, M. Heilmaier, A. Kauffmann, Creep behavior of a precipitation-strengthened A2-B2 refractory high entropy alloy, Acta. Mater. 288 (2025) 120827.
[19] X. Li, N. Saunders, A.P. Miodownik, The coarsening kinetics of γ′ particles in nickel-based alloys, Met. Mater. Trans. A 33 (2002) 3367–3373.
[20] Z.T. Kloenne, K. Kadirvel, J.-P. Couzinie, G.B. Viswanathan, Y. Wang, H.L. Fraser, High temperature phase stability of the compositionally complex alloy AlMo0.5NbTa0.5TiZr, Appl. Phys. Lett. 119 (2021) 151903.
[21] V. Soni, O.N. Senkov, B. Gwalani, D.B. Miracle, R. Banerjee, Microstructural design for improving ductility of an initially brittle refractory high entropy alloy, Sci. Rep. 8 (2018) 8816.
[22] S. Laube, S. Schellert, A. Srinivasan Tirunilai, D. Schliephake, B. Gorr, H.J. Christ, A. Kauffmann, M. Heilmaier, Microstructure tailoring of Al-containing compositionally complex alloys by controlling the sequence of precipitation and ordering, Acta. Mater. 218 (2021) 117217.
[23] S. Laube, H. Chen, A. Kauffmann, S. Schellert, F. Müller, B. Gorr, J. Müller, B. Butz, H.J. Christ, M. Heilmaier, Controlling crystallographic ordering in Mo–Cr–Ti–Al high entropy alloys to enhance ductility, J. Alloys. Compd. 823 (2020) 153805.
[24] C.A. Schneider, W.S. Rasband, K.W. Eliceiri, NIH image to ImageJ: 25 years of image analysis, Nat. Met. 9 (2012) 671–675.
[25] R.W. Cahn, P. Haasen, E.J. Kramer. Materials Science and Technology: A Comprehensive Treatment, The Classic Edition, Wiley, Weinheim, 2007.
[26] D.J. Larson, T.J. Prosa, R.M. Ulfig, B.P. Geiser, T.F. Kelly, Local Electrode Atom Probe Tomography, Springer, New York, 2013.
[27] H. Chen, A. Kauffmann, S. Seils, T. Boll, C.H. Liebscher, I. Harding, K.S. Kumar, D. V. Szabó, S. Schlabach, S. Kauffmann-Weiss, F. Müller, B. Gorr, H.-J. Christ, M. Heilmaier, Crystallographic ordering in a series of Al-containing refractory high entropy alloys Ta–Nb–Mo–Cr–Ti–Al, Acta. Mater. 176 (2019) 123–133.
[28] Y.Y. Zhao, H.W. Chen, Z.P. Lu, T.G. Nieh, Thermal stability and coarsening of coherent particles in a precipitation-hardened (NiCoFeCr)94Ti2Al4 high-entropy alloy, Acta. Mater. 147 (2018) 184–194.
[29] G. Song, Z. Sun, L. Li, X. Xu, M. Rawlings, C.H. Liebscher, B. Clausen, J. Poplawsky, D.N. Leonard, S. Huang, Z. Teng, C.T. Liu, M.D. Asta, Y. Gao, D.C. Dunand, G. Ghosh, M. Chen, M.E. Fine, P.K. Liaw, Ferritic alloys with extreme creep resistance via coherent hierarchical precipitates, Sci. Rep. 5 (2015) 16327.
[30] D.G. Morris, M.A. Muñoz-Morris, L.M. Requejo, New iron–aluminium alloy with thermally stable coherent intermetallic nanoprecipitates for enhanced high-temperature creep strength, Acta. Mater. 54 (2006) 2335–2341.
[31] P.A. Ferreirós, P.R. Alonso, G.H. Rubiolo, Effect of Ti additions on phase transitions, lattice misfit, coarsening, and hardening mechanisms in a Fe2AlV-strengthened ferritic alloy, J. Alloys. Compd. 806 (2019) 683–697.
[32] K. Ma, S. Cheng, X. Ma, T. Blackburn, A.J. Knowles, K. An, J. Santisteban, F. Sun, C. H. Zenk, P.A. Ferreirós, Lattice misfit design and characterisation in BCC superalloys, Scr. Mater. 267 (2025) 116802.
[33] M. Thomas, S. Naka, T. Khan, Stability of the B2 phase in ternary Ti–Al–X alloys (X=Nb, Mo, V), Mat. Trans. JIM 35 (1994) 787.
[34] D. Banerjee, The intermetallic Ti_2AlNb, Prog. Mater. Sci. 42 (1997) 135–158.
[35] F. Lu, S. Antonov, S. Lu, J. Zhang, L. Li, D. Wang, J. Zhang, Q. Feng, Unveiling the re effect on long-term coarsening behaviors of γ′ precipitates in Ni-based single crystal superalloys, Acta. Mater. 233 (2022) 117979.
[36] V.A. Vorontsov, J.S. Barnard, K.M. Rahman, H.-Y. Yan, P.A. Midgley, D. Dye, Coarsening behaviour and interfacial structure of γ′ precipitates in Co-Al-W based superalloys, Acta. Mater. 120 (2016) 14–23.
[37] S. Kumar, P. Pandey, K. Chattopadhyay, Influence of interfacial and strain energies on γ′ coarsening kinetics in complex concentrated alloys, Metals 33 (2024) 102018.
[38] S. Laube, A. Kauffmann, S. Schellert, S. Seils, A.S. Tirunilai, C. Greiner, Y. M. Eggeler, B. Gorr, H.-J. Christ, M. Heilmaier, Formation and thermal stability of two-phase microstructures in Al-containing refractory compositionally complex alloys, Sci. Technol. Adv. Mater. 23 (2022) 692–706.
[39] T. Philippe, P.W. Voorhees, Ostwald ripening in multicomponent alloys, Acta. Mat. 61 (2013) 4237.
[40] I.M. Lifshitz, V.V. Slyozov, The kinetics of precipitation from supersaturated solid solutions, J. Phys. Chem. Sol. 19 (1961) 35–50.
[41] T. Rieger, J.-M. Joubert, R. Poulain, X. Sauvage, E. Paccou, L. Perrière, I. Guillot, G. Dirras, G. Laplanche, M. Laurent-Brocq, J.-P. Couzinié, Influence of chemical composition on coarsening kinetics of coherent L12 precipitates in FCC complex concentrated alloys, J. Alloys. Compd. 967 (2023) 171711.
[42] M.Bonvalet Rolland, A. Borgenstam, Modeling precipitation kinetics in multicomponent alloys during deformation, Front. Mater. 9 (2022) 958472.
[43] J.Y.C. Fang, W.H. Liu, T. Yang, Y. Wu, Z.B. Jiao, Multicomponent precipitation and strengthening in intermetallic-strengthened alloys, Front. Mater. 9 (2022) 931098.
[44] I. Steinbach, Phase-field models in materials science, Model. Simul. Mat. Sci. Eng. 17 (2009) 073001.
[45] J. Zhang, C. Gadelmeier, S. Sen, R. Wang, X. Zhang, Y. Zhong, U. Glatzel, B. Grabowski, G. Wilde, S.V. Divinski, Zr diffusion in BCC refractory high entropy alloys: a case of 'non-sluggish' diffusion behavior, Acta. Mater. 233 (2022) 117970.
[46] A.M. Ges, O. Fornaro, H.A. Palacio, Coarsening behaviour of a Ni-base superalloy under different heat treatment conditions, Mat. Sci. Eng. 458 (2007) 96–100.
[47] M.R. Jahangiri, H. Arabi, S.M.A. Boutorabi, Comparison of microstructural stability of IN939 superalloy with two different manufacturing routes during long-time aging, Trans. Nonfer. Met. Soc. Chi. 24 (2014) 1717–1729.
[48] Y. Lu, J. Yamada, R. Miyata, H. Kato, K. Yoshimi, High-temperature mechanical behavior of B2-ordered Ti–Mo–Al alloys, Intermetallics 117 (2020) 106675.

[49] V. Gagneur, J.P. Magnussen, K. Ma, M.J. Lloyd, N. Martin, A.J. Knowles, Automated indentation-based slip trace analysis for bcc and B2 intermetallic plasticity, Mater. Charact. 229 (2025) 115524.
[50] F. Popille, J. Douin, Comparison of the deformation microstructures at room temperature in O and B2 phases of a Ti_2AlNb alloy, J. Phys. IV 06 (1996). C2-211-C2-216.
[51] K. Goyal, C. Bera, N. Sardana, Temperature-dependent structural, mechanical, and thermodynamic properties of B2-phase Ti_2AlNb for aerospace applications, J. Mater. Sci. 57 (2022) 19553–19570.
[52] D. Banerjee, A.K. Gogia, T.K. Nandi, V.A. Joshi, A new ordered orthorhombic phase in a Ti3AlNb alloy, Acta. Met. 36 (1988) 871–882.
[53] J.P. Couzinié, G.B. Viswanathan, V. Soni, R. Banerjee, H.L. Fraser, M.J. Mills, Unveiling the deformation mechanisms of BCC-superalloys, Scr. Mater. 267 (2025) 116801.
[54] G.B. Viswanathan, Z.T. Kloenne, J.P. Couzinié, B.A. Welk, S.J. Kuhr, H.L. Fraser, Deformation mechanisms and their role in the lack of ductility in the refractory-based high entropy alloy AlMo0.5NbTa0.5TiZr, Acta. Mater. 269 (2024).